Journal of Computational Physics 350 (2017) 638–656

Contents lists available at ScienceDirect

Journal of Computational Physics

www.elsevier.com/locate/jcp

Fully-resolved simulation of particulate flows with particles–fluid heat transfer

Yayun Wang [a], Adam J. Sierakowski [a], Andrea Prosperetti [b,c,*]

[a] Department of Mechanical Engineering, Johns Hopkins University, 3400 North Charles Street, Baltimore, MD 21218-2681, USA
[b] Department of Mechanical Engineering, University of Houston, 4726 Calhoun Rd, Houston, TX 77204-4006, USA
[c] Faculty of Science and Technology and J.M. Burgers Centre for Fluid Dynamics, University of Twente, P.O. Box 217, 7500 AE Enschede, The Netherlands

ARTICLE INFO

Article history:
Received 26 October 2016
Received in revised form 16 May 2017
Accepted 24 July 2017
Available online 24 August 2017

Keywords:
Heat transfer in particulate flows
Physalis method
Fully-resolved simulations of extended particles

ABSTRACT

The PHYSALIS method for the fully-resolved simulation of particulate flows is extended to include heat transfer between the particles and the fluid. The particles are treated in the lumped capacitance approximation. The simulation of several steady and time-dependent situations for which exact solutions or exact balance relations are available illustrates the accuracy and reliability of the method. Some examples including natural convection in the Boussinesq approximation are also described.

1. Introduction

The last decade has witnessed a great interest in the fully-resolved simulation of flows with many suspended particles. The majority of these studies use some variant of the immersed boundary method, notable examples being the work of Uhlmann and co-workers (see e.g. [42,14,19]), Kempe and Froehlich (see e.g. [18,29]), Breugem, Brandt and co-workers (see e.g. [26,25,13]) and many others. Several other approaches have also been developed including the fictitious domain, lattice Boltzmann and discrete element methods (see e.g. [43,15,48,8]).

In contrast, the related problem of heat transfer in particulate flows has received much less attention. Several papers that adopt the point-particle or discrete-element models are available (see e.g. [49,2]), but it is only very recently that truly fully-resolved multi-particle simulations have started to appear in the literature. While a few of these studies rely on the lattice Boltzmann method (see e.g. [34,21]) or others [10,11], the vast majority of them employ the immersed boundary method for both the momentum and the energy equation (see e.g. [7,40,41,46,12,47,38]).

Deen et al. [7] describe a direct-forcing method in which a parabolic interpolation connects the temperature on the boundary to that at two neighboring grid points along a line. This method encounters difficulties when different temperature values can be attached to the same grid point by following different lines. In a later study from the same group [40], the procedure was improved by borrowing the method developed by Uhlmann [42] for the momentum equation: the energy equation is augmented by forcing terms which enforce the temperature boundary condition by means of regularized delta functions. A similar approach had been developed by Wang et al. [44] for the two-dimensional case. Xia et al. [46] extended the method to three dimensions, but they concluded that the discretization necessary for accuracy was too fine to make

* Corresponding author at: Department of Mechanical Engineering, University of Houston, 4726 Calhoun Rd, Houston, TX 77204-4006, USA.
E-mail address: aprosperetti@uh.edu (A. Prosperetti).

http://dx.doi.org/10.1016/j.jcp.2017.07.044
0021-9991/

the method practical. For this reason, they switched to the ghost-cell immersed boundary method introduced in [24] and extended in [33]. Even with this improvement, they found that more than 30 cells per particle diameter were needed to accurately calculate the heat transfer from a single particle immersed in a stream with a Reynolds number of 100. Similar or finer levels of discretization have been found necessary also in the methods of [41] and [38].

In earlier work we have developed PHYSALIS, an alternative method for the solution of the momentum equations, based on the use of local analytic solutions as "bridges" between the particle surfaces and a fixed underlying Cartesian grid (see e.g. [16,36]). The method has several advantages including the possibility of achieving an excellent accuracy with a relatively coarse discretization. In this work we describe an extension of the same approach to the energy equation for an incompressible fluid and encounter similar beneficial features. Although the fluid properties are considered constant, natural convection is included in the Boussinesq approximation. The particle Biot number is assumed to be small so that a lumped-capacitance treatment of the particles is justified, although extensions to other cases are also possible.

After stating the mathematical problem in the next section, we provide in section 3 a synthetic overview of the PHYSALIS method for momentum. We then describe its extension to the energy equation (section 4) and describe its implementation (section 5). Section 6 provides a verification of the method with several examples with fixed particles. In the final section we show examples in which the particles can move under the action of buoyancy-induced convection.

2. Mathematical formulation

We consider spherical particles in a non-isothermal, incompressible Newtonian fluid under conditions such that the Boussinesq approximation is applicable. The Navier–Stokes equations then take the form

$$\nabla \cdot \mathbf{u} = 0\,, \tag{1}$$

$$\frac{\partial \mathbf{u}}{\partial t} + \mathbf{u}\cdot\nabla\mathbf{u} = -\frac{1}{\rho}\nabla p + \nu\nabla^2\mathbf{u} - \beta T\mathbf{g}\,. \tag{2}$$

Here $\mathbf{u}$ is the velocity field, p the pressure in excess of a mean hydrostatic pressure, T the temperature in excess of some constant reference temperature T_{ref} (so that, here and in the following, in reality T stands for $T - T_{ref}$) and $\mathbf{g}$ the acceleration of gravity. The fluid density is denoted by ρ, the kinematic viscosity by ν and the thermal expansion coefficient by β. The energy equation is

$$\frac{\partial T}{\partial t} + \mathbf{u}\cdot\nabla T = D\nabla^2 T\,, \tag{3}$$

with $D = k/(\rho c_p)$ the thermal diffusivity of the fluid; k and c_p are the fluid thermal conductivity and specific heat, respectively. Following the standard procedure in the Rayleigh–Bénard literature, the contribution of the dissipation function (i.e., viscous heating) is neglected here on account of the smallness of this effect.

For the particles we adopt a simple lumped-capacitance model according to which the particle temperature T_p is governed by

$$\tau_p \frac{dT_p}{dt} = -\frac{a}{s_p}\oint_{s_p} \nabla T\cdot\mathbf{n}_p ds_p\,. \tag{4}$$

Here a is the particle radius, $s_p = 4\pi a^2$ is the particle surface, $\mathbf{n}_p$ the outwardly-directed unit normal and

$$\tau_p = \frac{\rho_p c_{pp} a^2}{3k}\,, \tag{5}$$

is the particle thermal time constant; here ρ_p and c_{pp} are the particle density and specific heat and k is the fluid thermal conductivity. The right-hand side of (4) is the integral of the normal fluid temperature gradient evaluated at the particle surface.

3. General description of the PHYSALIS method

All fixed-grid methods for particulate flows face the difficulty of reconciling the geometry of the particle surface, on which boundary conditions are imposed, with the underlying non-conforming grid. In the PHYSALIS method this problem is solved by using an analytic solution of the field equations locally valid in the immediate neighborhood of the particle as a "bridge" between the particle surface and the adjacent grid points. As an introduction to how the basic idea is applied to the energy equation we provide here a synthetic description of its application to the (isothermal) Navier–Stokes equations; a detailed description is available in several previous papers [16,36].

For simplicity we start by considering the case of a single particle stationary in a flowing fluid. Because of the no-slip condition, the fluid at the particle surface is also stationary and, therefore, its velocity very near the particle will be small. This circumstance allows us to linearize the Navier–Stokes equations around the state of zero motion reducing them, in effect, to the Stokes equations. Of course, away from this thin region (in practice, at distances from the particle surface of

the order of the mesh length of the finite-difference discretization) inertia is important and the full Navier–Stokes equations must be solved. The Stokes equations for a spherical boundary admit a general solution, first given by Lamb [22] (see also [20]), which somewhat symbolically may be written as

$$p(\mathbf{x},t) = \sum_{\ell=1}^{\infty}\sum_{m=-\ell}^{\ell} P_{\ell m}(t)\, p_{\ell m}(\mathbf{x})\,, \qquad \mathbf{u}(\mathbf{x},t) = \sum_{\ell=1}^{\infty}\sum_{m=-\ell}^{\ell} U_{\ell m}(t)\,\mathbf{u}_{\ell m}(\mathbf{x})\,. \tag{6}$$

The precise form of the velocity expansion is somewhat different (see e.g. [36]), but for simplicity we write it in this form which is sufficient to explain the principle of the method. The functions $p_{\ell m}$ and $\mathbf{u}_{\ell m}$ are explicitly known in terms of spherical harmonic expansions. In particular, the $\mathbf{u}_{\ell m}$ satisfy exactly the no-slip condition on the particle surface whatever the level of truncation of the infinite summations. At each time step, the time-dependent coefficients $P_{\ell m}(t)$ and $U_{\ell m}(t)$ are adjusted to match the local solution (6), valid in the immediate neighborhood of the particle, to the fully non-linear finite-difference solution. In practice, the infinite summations are truncated at $\ell = \ell_{max}$ which results in the retention of $3\ell_{max}(\ell_{max}+2)+1$ coefficients (the abbreviated notation $U_{\ell m}$ used in (6) actually involves two families of coefficients in addition to the $P_{\ell m}(t)$). Typical values used in our simulations are $\ell_{max} = 2$ or 3, which result in 25 and 46 coefficients per particle, respectively.

The time advancement of the solution proceeds as follows:

1. Start from a provisional finite-difference solution, typically the solution at the previous time step;
2. By taking suitable scalar products of this solution on a spherical integration surface of radius r_s concentric with the particle, determine the coefficients $P_{\ell m}$ and $U_{\ell m}$. For example, $P_{\ell m}$ would be determined from
$$P_{\ell m} = \left(Y_\ell^m,\ p(\mathbf{x},t)|_{|\mathbf{x}|=r_s}\right) = \int_\Omega \overline{Y}_\ell^m\, p(r_s,\theta,\phi)\, d\Omega\,, \tag{7}$$
in which the overline denotes the complex conjugate, θ and ϕ are the angular variables in a local spherical coordinate system centered at the particle center and Ω is the solid angle with $d\Omega = \sin\theta\, d\theta\, d\phi$;
3. Use (6) with the coefficients thus determined to assign pressure boundary conditions (relative to a level arbitrarily set to zero) and velocity boundary conditions and on a "cage" of nodes adjacent to the particle surface;
4. Solve the Navier–Stokes equations over the finite-difference grid subject to these assigned velocity boundary conditions on the cage nodes; the pressure satisfies homogeneous Neumann conditions on the outer surface of the domain and Dirichlet conditions on the cage nodes; the use of these Dirichlet conditions is one respect in which the present method differs from the standard projection-method as discussed in [36];
5. Repeat to convergence.

The procedure for moving particles can be reduced to that of stationary particles by a change of the reference frame and a simple explicit transformation of the dependent variables (see e.g. [36], and equation (8) below).

There are two reasons why the coefficients determined at step 2 will be different in two successive iterations until the Stokes and Navier–Stokes solutions agree in the immediate neighborhood of the particle. In the first place, the solution (6) contains information on four scalar functions, the pressure and the three velocity components, and three additional scalar functions can be derived by calculating the vorticity of the flow. A proper count of the coefficients synthetically indicated by $P_{\ell m}$ and $U_{\ell m}$ in (6) shows that there are in fact three families of coefficients, and the fact that three families are sufficient to express 7 scalar functions is of course a consequence of the fact that these functions are not independent but are related to each other by the Stokes equations. If the coefficients are incorrect, the 7 scalar functions will be incompatible and this incompatibility will generate different values of the coefficients at the next iteration. Secondly, the coefficients are found on the basis of the field values on the surface of radius r_s over which the scalar product is evaluated. The expressions (6) with the coefficients thus determined are compatible with the velocity values at the cage nodes, where the boundary conditions are applied, only if the equations are satisfied; again, the lack of compatibility that persists until convergence is achieved contributes to the difference between the coefficient values at two successive iterations.

In the case of potential flow, studied in [27], a single family of coefficients is sufficient to determine the flow and the difference between two successive iterations is only due to the second factor. As will be shown in the next section, the same situation is encountered with the energy equation in which the temperature field is described by a single family of coefficients.

In extending the method to the non-isothermal case with the Boussinesq approximation, one slight adjustment needs to be made in the way in which the momentum equation is reduced to the Stokes form. In the isothermal case, in transforming the frame of reference to the rest frame of the particle, it is necessary to introduce a modified pressure field $\tilde{p}$ according to

$$\tilde{p} = p + \rho(\dot{\mathbf{w}} - \mathbf{g})\cdot\mathbf{r} - \frac{1}{2}\rho\,(\boldsymbol{\Omega}\times\mathbf{r})^2\,, \tag{8}$$

in which $\dot{\mathbf{w}}$ and $\boldsymbol{\Omega}$ are the instantaneous acceleration and angular velocity of the particle and $\mathbf{r}$ is the position vector with respect to the particle center. This step is necessary to eliminate some of the terms arising from the change of reference

frame from the right-hand side of the momentum equation (2). Due to the adoption of the Boussinesq approximation, in order to reduce the right-hand side of the momentum equation to the Stokes form, it is necessary to eliminate the new Boussinesq term involving the temperature as well. In the immediate neighborhood of the particle this objective can be achieved very simply, if approximately, by replacing T by the particle temperature T_p modifying (8) to

$$\tilde{p} = p + \rho(\dot{\mathbf{w}} - \mathbf{g}) \cdot \mathbf{r} - \frac{1}{2}\rho\,(\boldsymbol{\Omega} \times \mathbf{r})^2 - \beta\rho T_p \mathbf{g} \cdot \mathbf{r}\,. \tag{9}$$

The error incurred with this approximation is small as the temperature in the neighborhood of the particle is close to T_p and the fluid volume over which the approximation is applied is a thin layer near the particle. A quantitative estimate of this error is provided in the next section. It would also be possible to modify the Lamb solution so as to allow for a spatially varying temperature field, but the necessary analytical and computational effort would be substantial and seems unwarranted given the smallness of the error.

4. The local solution

Due to the invariance of the convective derivative upon a change of the reference frame, the velocity $\mathbf{u}$ in (3) can be considered as the velocity in the rest frame of the particle. This velocity vanishes at the particle surface and, therefore, the convective term $\mathbf{u} \cdot \nabla T$ will be very small near the particle surface so that (3) can be simplified to

$$\frac{\partial T}{\partial t} = D\nabla^2 T\,. \tag{10}$$

Changes in the value of the particle temperature reach a distance l in the fluid after a time of the order of l^2/D. If this time lag is much smaller than the time scale for the variation of the particle surface temperature, the time derivative can also be dropped and the equation simply becomes

$$\nabla^2 T = 0\,. \tag{11}$$

The consequences of this quasi-steady approximation will be considered further below and a way to partially correct for the error incurred described.

The solution of (11) satisfying the condition $T = T_p^\alpha$ on the surface $|\mathbf{x} - \mathbf{x}^\alpha(t)| = a$ of the α-th particle instantaneously centered at $\mathbf{x}^\alpha(t)$ is given by

$$T(\mathbf{x}, t) = T_p^\alpha(t) + \sum_{\ell=1}^{\infty}\left[\left(\frac{r}{a}\right)^\ell - \left(\frac{a}{r}\right)^{\ell+1}\right]\sum_{m=-\ell}^{\ell} T_{\ell m}(t) Y_\ell^m(\theta, \phi)\,, \tag{12}$$

with $r = |\mathbf{x} - \mathbf{x}^\alpha(t)|$, the Y_ℓ^m spherical harmonics and the $T_{\ell m}(t)$ coefficients to be determined in such a way that the local solution (12) matches the solution of the complete energy equation (3). It will be noted that (12) satisfies the correct boundary condition at the particle surface irrespective of the order of truncation of the infinite sums. The Nusselt number at the particle surface, defined by

$$Nu_p = \frac{Q_p}{2\pi a k T_p}\,, \tag{13}$$

in which Q_p is the total heat flowing out of the particle,

$$Q_p \equiv -\oint_{S_p} k\nabla T \cdot \mathbf{n}_p ds_p\,, \tag{14}$$

is expressed in terms of the first coefficient T_{00} of the expansion (12) as

$$Nu_p = -\frac{T_{00}(t)}{\sqrt{\pi}\,T_p}\,. \tag{15}$$

The reader is reminded of the fact that, throughout this paper, T denotes the temperature in excess of some reference value.

The coefficients $T_{\ell m}(t)$ bear to the fluid temperature field evaluated on a spherical surface of radius r_T concentric with the particle a relation similar to that shown in (7), namely

$$\begin{aligned}\left[\left(\frac{r_T}{a}\right)^\ell - \left(\frac{a}{r_T}\right)^{\ell+1}\right] T_{\ell m}(t) &= \left(Y_\ell^m, [T(\mathbf{x}, t) - T_p(t)]_{|\mathbf{x}|=r_T}\right) \\ &= \int_\Omega \overline{Y}_\ell^m [T(r_T, \theta, \phi) - T_p(t)] d\Omega\,.\end{aligned} \tag{16}$$

It may be noted that there is no reason why the radius r_T of the integration surface used here should equal r_s used for the evaluation of the momentum integrals.

An approximate way to account for the omission of the time derivative in (10) consists in setting $T = T_0 + T_1$ with T_0 satisfying the steady equation (11) and T_1 satisfying

$$D\nabla^2 T_1 \simeq \frac{\partial T_0}{\partial t} \,. \tag{17}$$

Since T_0 already accounts for the particle temperature at the particle surface and the fluid temperature on the integration surface $r = r_T$, the solution T_1 of (17) must vanish on these two surfaces. Upon substitution of (12) for T_0 in the right-hand side, the equation can be solved with the result

$$\begin{aligned} T_1 = \sum_{\ell=1}^{\infty}\sum_{m=-\ell}^{\ell}\Bigg[&\left(r^{\ell+2} - \frac{r^\ell a^2(s^{2\ell+3}-1)}{s^{2\ell+1}-1} + \frac{a^{2\ell+3}s^{2\ell+1}(s^2-1)}{r^{\ell+1}(s^{2\ell+1}-1)}\right)A_{\ell m} \\ &-\left(r^{-\ell+1} - \frac{r^\ell(s^2-1)}{a^{2\ell-1}(s^{2\ell+1}-1)} + \frac{a^2(s^2-s^{2\ell+1})}{r^{\ell+1}(s^{2\ell+1}-1)}\right)B_{\ell m}\Bigg] Y_\ell^m(\theta,\phi)\,, \end{aligned} \tag{18}$$

in which $s = r_T/a$. The coefficients $A_{\ell m}(t)$ and $B_{\ell m}(t)$ are given by

$$A_{\ell m} = \frac{\dot{I}_{lm}}{Da^\ell} + \frac{\sqrt{4\pi}}{D}\dot{T}_p\delta_{\ell 0}\,, \qquad B_{\ell m} = \frac{a^{\ell+1}}{D}\dot{T}_{lm}\,, \tag{19}$$

where the superposed dots denote time derivatives. The correction to the temperature gradient at the particle surface is

$$\begin{aligned} \left.\frac{\partial T_1}{\partial r}\right|_{r=a} &= \sum_{\ell=1}^{\infty}\sum_{m=-\ell}^{\ell}\Bigg[\frac{(2\ell+3)s^{2\ell+1} - (2\ell+1)s^{2\ell+3} - 2}{s^{2\ell+1}-1}a^{\ell+1}A_{\ell m} \\ &\qquad -\frac{2s^{2\ell+1} - (2\ell+1)s^2 + 2\ell - 1}{a^\ell(s^{2\ell+1}-1)}B_{\ell m}\Bigg] Y_\ell^m(\theta,\phi) \\ &\simeq (s-1)\sum_{\ell=1}^{\infty}\sum_{m=-\ell}^{\ell}\left[(2\ell+3)a^{\ell+1}A_{\ell m} - \frac{2\ell-1}{a^\ell}B_{\ell m}\right]Y_\ell^m(\theta,\phi)\,, \end{aligned} \tag{20}$$

where the validity of the approximation in the last step rests on the fact that, in practice, the summation is limited to relatively small values of ℓ. Since the maximum value of $s-1$ is of the order of $\Delta x/a$, with Δx the mesh length, this correction to the heat flux at the particle surface is small as long as the temperature rate of change is moderate, which is a pre-requisite for the applicability of the present model.

The error incurred in replacing T by T_p in the Boussinesq term very near the particle in (9) can now be estimated. If the quasi-steady approximation (12) is used without the correction (18), we define

$$\epsilon_0 = \frac{1}{T_p v_p(s^3-1)}\int_a^{r_T} r^2 dr \int_\Omega \left(T_0 - T_p\right) d\Omega\,, \tag{21}$$

with $v_p = \frac{4}{3}\pi a^3$ the particle volume, so that $v_p(s^3-1)$ is the volume of the shell between the sphere of radius r_T and the particle surface where the temperature is incorrectly evaluated. The result is

$$\epsilon_0 = \frac{1}{2\sqrt{4\pi}}\frac{(2s+1)(s-1)}{s^2+s+1}\frac{T_{00}}{T_p} = -\frac{1}{4}\frac{(2s+1)(s-1)}{s^2+s+1}Nu_p\,. \tag{22}$$

This quantity represents the relative error made in estimating the buoyancy in the spherical shell between the particle surface and the temperature integration surface. If α denotes the particle volume fraction, this error is incurred over a fraction of the total volume given by $\alpha(s^3-1)$ which is small even for relatively large volume fractions. By including the correction (18), ϵ_0 is augmented by

$$\begin{aligned} \epsilon_1 &\equiv \frac{1}{T_p v_p(s^3-1)}\int_a^{r_T} r^2 dr \int_\Omega T_1 d\Omega \\ &= -\frac{(s-1)^2a^2}{20\sqrt{4\pi}(s^3-1)DT_p}\left[(s-1)(8s^2+9s+3)\dot{T}_{00} + \frac{1}{\sqrt{\pi}}(4s^2+7s+4)\dot{T}_p\right], \end{aligned} \tag{23}$$

which is again small as long as the temperature rate of change is moderate.

As a concluding comment it may be noted that, in place of (12) or (18), one could use the exact solution of the diffusion equation (10) which, however, would involve a convolution integral and make the calculation significantly more complex. Secondly, the form (12) of the local solution is suitable when the particle surface temperature is spatially uniform as assumed here with the use of the lumped capacitance approximation. A similar expansion can be written down whatever the particle surface temperature distribution. However, if the time scale for temperature homogenization in the particle cannot be neglected, it becomes necessary to solve the conduction equation inside the particle and, again, the complexity of the calculation increases significantly.

5. Implementation

Here we describe a straightforward implementation of the mathematical model formulated in the previous section. Since much of it is the same as for the isothermal PHYSALIS implementation, which is described in detail in several earlier papers [16,35,36], we focus here mainly on the novel aspects that are introduced by the energy equation.

The momentum and energy equations are discretized on a staggered uniform grid with second-order spatial accuracy. Time stepping is first-order accurate and explicit, which requires a limitation on the time step Δt given by

$$\Delta t = \frac{C}{\frac{\max|u_i|}{\Delta x} + \frac{2\min(\nu, D)}{\Delta x^2}}\,. \tag{24}$$

The maximum is over all the velocity components at all the nodes; the constant C is typically taken as 0.5. To insure that the expansions for the flow and temperature fields are used within their domain of validity, the grid size Δx must be chosen of the order of $a/\sqrt{Re}$ (as explained in our earlier papers, e.g. [36]) and of the order of $a/\sqrt{Pe}$, with Re and Pe the Reynolds and Péclet numbers based on the particle diameter.

The scalar products in (16) are effected by the same Lebedev quadrature method used e.g. for (7) and described in [35] and [36]. The temperature at the quadrature nodes is obtained by linear interpolation from the surrounding nodes. This step has only first-order accuracy, which reduces somewhat the second-order accuracy used in the spatial discretization. When two particles are very close one (or a very small number) of quadrature nodes may fall inside the other particle. To deal with this situation, the temperature at all the interior nodes is set equal to the particle temperature T_p. The summation in (12) is truncated at a maximum value ℓ_{max}, which results in $(2\ell_{max}+1)^2$ coefficients $T_{\ell m}$.

The calculation proceeds according to the following steps:

1. First the velocity and pressure fields are updated using the previous-time temperature according to the procedure described in section 3; the particle position is also updated;
2. For simplicity, as in [5], the particle temperature is updated by a first-order Euler discretization of (4):

$$T_p^{n+1} = T_p^n - \frac{1}{\tau s_p}\oint_{s_p} \nabla T^n \cdot \mathbf{n}_p ds_p = T_p^n - \frac{\Delta t}{\tau\sqrt{4\pi}} T_{00}^n\,, \tag{25}$$

   with superscripts indicating the time level;
3. Eq. (12) with the updated T_p^{n+1} and the previous-time values of the coefficients $T_{\ell m}$ is used to assign the temperature at the cage nodes (which are the same as the cage nodes for the pressure field);
4. The energy equation is solved with these boundary conditions and appropriate boundary conditions on the outer surface of the computational domain; the updated velocity field of step 1 is used in the energy equation;
5. From the temperature solution thus obtained a new set of coefficients $T_{\ell m}$ is found by taking the appropriate scalar products (16), the temperature at the cage nodes is updated and, starting with step 3, the procedure is repeated to convergence of the $T_{\ell m}$.

As explained before, the expression (12) describes the temperature both on the integration surface and at the cage nodes only if the temperature coefficients are correct. As long as there is a difference between these temperatures the coefficients will change for every iteration. For this difference to manifest itself in a robust way it is necessary that some distance exist between the integration surface and the cage nodes. However, if this distance is too large, the assumption of steady local conduction will be violated and there may be an interference with neighboring particles. It is argued below at the end of section 6.2 on the basis of our numerical experience that r_T/a is best chosen somewhere between $1+\Delta x/a$ and $1+2\Delta x/a$.

6. Verification

We describe here the results of several tests of the accuracy of our method and of its implementation. Some examples are based on exact analytic solutions and others on the exact integral balance relations derived in the Appendix.

6.1. Stationary particle in a quiescent fluid

The simplest case is that of a single stationary particle in a quiescent fluid. We begin by considering an overall energy balance between the particle and the outer surface S_f of the computational domain. In steady conditions, Q_p, the heat flow

Table 1
The deviation from 1 of the quantity Λ_T, defined in (26), is a measure of the error affecting the solution of the energy equation. The results in this table illustrate the sensitivity of the numerical error to the choice of the radius r_T/a of the integration surface and to different orders of truncation ℓ_{max} of the series expansion (12). The situation simulated is a single particle at constant temperature centered in a cubic enclosure subject to a constant heat flux with no fluid flow. The particle occupies 6.5% of the box volume.

r_T/a	ℓ_{max}	Λ_T
1.15	2, 3	1.00393
1.15	4	1.00229
1.2	2, 3	1.00345
1.2	4	1.00226
1.25	2, 3	0.99399
1.25	4	0.99329

out of the particle defined in (14), should equal the total heat flowing out of the computational domain (see Eq. (A.5) in the Appendix) so that the ratio defined by

$$\Lambda_T = -\frac{1}{Q_p}\oint_{S_f} k\nabla T\cdot\mathbf{n}dS_f\,, \tag{26}$$

should equal 1 in the absence of errors. In the situation we consider a uniform heat flux is imposed on one of the outer faces of the computational domain, all the other faces being insulated, and the particle temperature is held fixed as might be the case, for example, for a particle undergoing melting or freezing.

Table 1 shows the computed values of Λ_T for different truncation orders ℓ_{max} of the infinite sum (12) and different radii r_T/a of the integration surface for the scalar products (16). Here we use eight cells per radius. The error is consistently found to be a fraction of 1% and essentially insensitive to the details of the computation.

Next we consider three situations chosen so as to investigate the error incurred with the simple quasi-steady approximation (12) and the effectiveness of the correction (18). We compare the computed results with the analytic solution corresponding to a fluid at the reference temperature far from the particle. The computational domain is a cube of side $16a$ with the particle centered at its center. On the cube surfaces the reference temperature is imposed since, up to the maximum times considered here, they are far enough from the particle that the difference with the analytic solution is negligible. In these simulations we use $a/\Delta x = 8$, $r_T/a = 1.15$ and $\ell_{max} = 3$.

In the first case the fluid is initially at the reference temperature while the particle temperature takes on the value T_p at $t = 0+$. The analytic solution for the fluid temperature is

$$\frac{T(r,t)}{T_p} = \frac{a}{r}\mathrm{erfc}\left(\frac{r-a}{2\sqrt{Dt}}\right), \tag{27}$$

and the corresponding Nusselt number at the particle surface defined in (13) is

$$Nu_p = \frac{Q_p}{2\pi akT_p} = 2 + \frac{2a}{\sqrt{\pi Dt}}, \tag{28}$$

with Q_p as in (14).

In the second example the particle temperature is a linearly increasing function of time, $T_p = t$. The analytic solution for the fluid temperature is readily found by means of the Laplace transform and is

$$T(r,t) = \left(t + \frac{(r-a)^2}{2D}\right)\frac{a}{r}\mathrm{erfc}\left(\frac{r-a}{2\sqrt{Dt}}\right) - \frac{a(r-a)}{r}\sqrt{\frac{t}{\pi D}}\exp\left(-\frac{(r-a)^2}{4Dt}\right). \tag{29}$$

For the third example the particle temperature is a sinusoidal function of time oscillating with an angular frequency ω and an amplitude T_A. When steady conditions have been reached, the analytic solution for the fluid temperature is the real part of

$$T(r,t) = \frac{a}{r}\exp\left(i\omega t - \sqrt{\frac{i\omega}{D}}(r-a)\right)T_A\,. \tag{30}$$

Figs. 1 and 2 refer to the first example. The first figure shows a comparison of the computed temperature field (symbols) superimposed on the analytic solution (27) (continuous lines) at various instants of time. One observes an excellent agreement at the times shown. At very early times, however, one expects some error which, indeed, is evident in Fig. 2. Here the particle Nusselt number is shown as a function of time with a focus on the early times. In this extreme case in which the time scale for the temperature variation of the particle is as short as possible – in fact, zero – the error is not small, but it

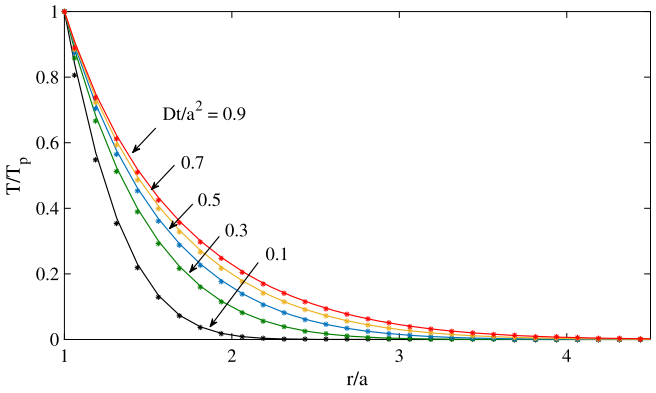

Fig. 1. Temperature distribution in the neighborhood of a particle instantaneously brought to the temperature T_p higher than that of the surrounding medium which is at the reference temperature. The lines (in ascending order with increasing time) are the analytic solution (27) and the symbols the computed results.

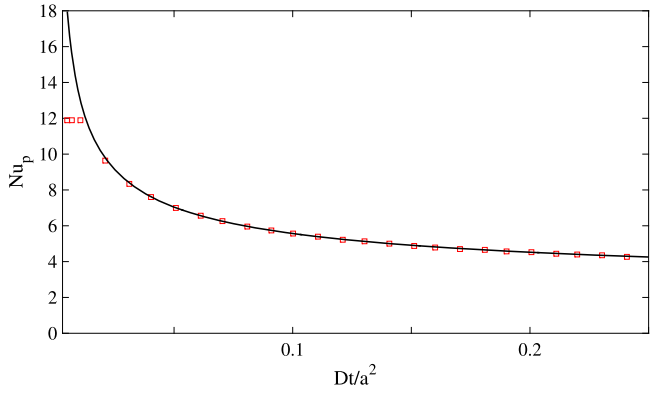

Fig. 2. Early-time behavior of the particle Nusselt number for the situation of the previous figure. The line is the exact solution (28) and the symbols the numerical results.

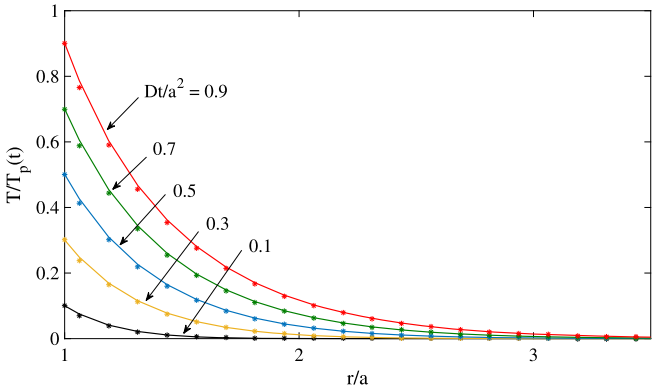

Fig. 3. Temperature distribution in the neighborhood of a particle the temperature of which increases linearly with time. Initially both the particle and the medium surrounding it are at the reference temperature. The lines (in ascending order with increasing time) are the analytic solution (29) and the symbols the computed results.

very quickly decreases. The dimensionless time for the propagation of temperature information over a distance comparable to a mesh length away from the particle surface is of the order of $Dt/a^2 = (\Delta x/a)^2$ which, with $a/\Delta x = 8$ as used here, is about 0.0156. The figure shows that, after a time of this order, the error has indeed become negligible.

Fig. 3 refers to the second example, with a linearly increasing particle temperature. Here the temperature change is gradual and the numerical and analytical solutions are always very close.

The third example, oscillating particle temperature, offers us the possibility of modulating between a very short time scale (large ω) and a long one. Fig. 4 shows the results for a case with a dimensionless frequency, or Péclet number

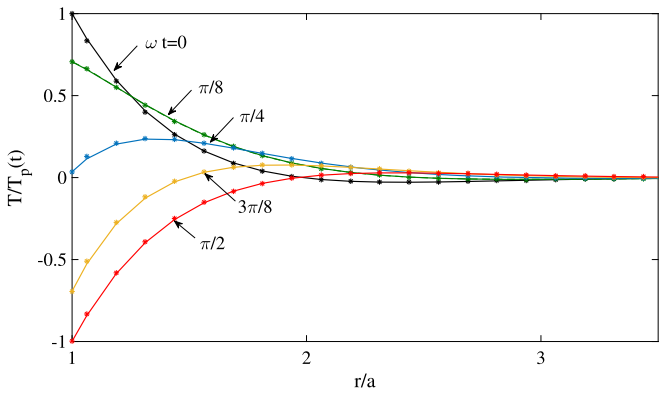

Fig. 4. Steady-state temperature distribution in the medium surrounding a particle the temperature of which oscillates in time with a frequency ω at different instants of time. The Péclet number is $\omega a^2/D = 5$. The lines are the exact solution (30) and the symbols the computational results.

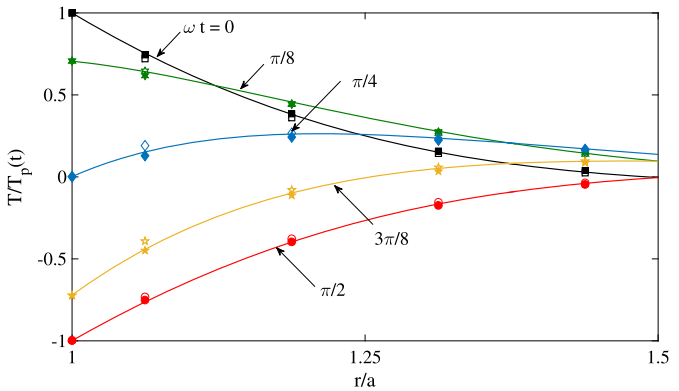

Fig. 5. Steady-state temperature distribution in the medium surrounding a particle the temperature of which oscillates in time with a frequency ω at different instants of time. The Péclet number is $\omega a^2/D = 20$. The lines are the exact solution (30), the open symbols the computational results found using (12) for the temperature at the temperature cage nodes, and the filled symbols the computational results found by adding the correction (18) to the temperature at the cage nodes.

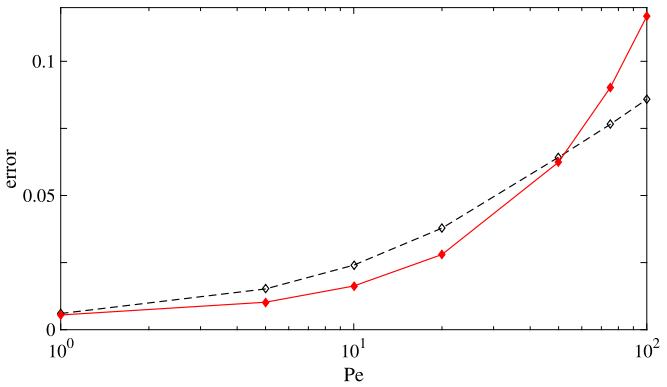

Fig. 6. Cumulative error, defined in (31) of the corrected (solid line) and uncorrected numerical result for a particle the surface temperature of which oscillates sinusoidally. The horizontal axis is the Péclet number $Pe = \omega a^2/D$.

$Pe = \omega a^2/D = 5$. Agreement between the analytical and computational results (lines and symbols, respectively) is essentially perfect. If the dimensionless frequency is increased to $Pe = 20$ as in Fig. 5, however, one notices some errors of the quasi-steady approximation (open symbols). The filled symbols show the results after the application of the correction T_1 given in (18). The difference is small, but it somewhat improves the agreement. Fig. 6 is a graph of the error of the numerical solution with respect to the analytical one as a function of the Péclet number. The error ϵ shown here is defined as

Table 2
The deviation from 1 of the quantity Λ_T, defined in (26) is a measure of the error affecting the solution of the energy equation. N_p is the number of particles; r_T is the radius of the integration surface for the temperature; ℓ_{max} is the maximum order of Lamb coefficients retained in the temperature expansion; α is the particle volume fraction; $a/\Delta x$ is the number of cells per radius a; the other quantities are defined in Fig. 7.

N_p	r_T/a	ℓ_{max}	$a/\Delta x$	α	D_c/a	D_{left}/a	D_{top}/a	Λ_T
2	1.15	2	8	0.177	0.5	0.375	0.5	1.0201
2	1.15	4	8	0.177	0.5	0.375	0.5	1.0103
2	1.15	4	8	0.282	0.25	0.25	0.25	0.96598
2	1.15	4	16	0.282	0.25	0.25	0.25	1.0041
2	1.08	4	16	0.368	0.25	0.125	0.125	0.98457
2	1.04	4	32	0.368	0.25	0.125	0.125	0.99741
10	1.15	4	8	0.250	–	random	–	1.0083
10	1.15	4	16	0.250	–	random	–	1.0020
10	1.08	4	16	0.250	–	random	–	1.0017
27	1.08	4	16	0.368	0.25	0.125	0.125	1.0089
27	1.04	4	16	0.368	0.25	0.125	0.125	1.0288

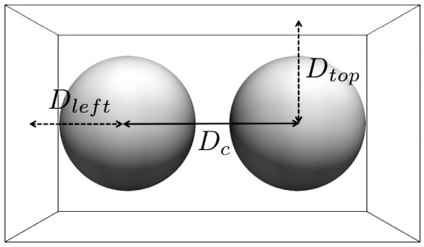

Fig. 7. Illustration of the geometry used for the simulations of Table 2.

$$\epsilon = \frac{1}{T_A}\sqrt{\sum_{i=1}^{N_{pnts}} \left\langle [T_{num}(\mathbf{x}_i,t) - T_{ex}(\mathbf{x}_i,t)]^2 \right\rangle}, \tag{31}$$

where the $N_{pnts} = 56$ points $\mathbf{x}_i$ are taken along a line through the sphere center and perpendicular to one of the sides of the enclosure and the angle brackets indicate the average over one cycle of oscillation. The solid and dashed lines are the errors affecting the corrected and uncorrected numerical results. It can be seen that the correction is beneficial up to $Pe \sim 50$, but becomes detrimental for larger values of Pe. This feature is due to the fact that, at frequencies of this order, the phase of the temperature oscillation reverses during the diffusion time over a distance of the order of the mesh length $(\Delta x)^2/D$. Indeed $\omega(\Delta x)^2/D \sim 1$ is equivalent to $Pe \sim (a/\Delta x)^2$ which, with the present parameter values, is $Pe \sim 64$.

6.2. Several stationary particles in a quiescent fluid

In Table 2, we show results similar to those of Table 1 for several particles and different volume fractions. The geometry used for the two-particles simulations is shown in Fig. 7 where also the symbols D_c, D_{left} and D_{top} are defined. A similar domain is used for the ten-particles simulation while that for 27 regularly arranged particles is a cube. In all cases a uniform heat flux is prescribed on the left vertical face while all other faces are insulated. The particle temperatures are prescribed and held fixed. The particle positions are held fixed while the number of cells and r_T/a are changed.

It is clear from the table that the accuracy of the results is mostly dependent on the number of cells between the particle surface and the closest particle or the closest boundary of the domain, which decreases with increasing volume fraction. The accuracy of the simulation increases as the number of cells n_c in the smallest of these gaps is increased. So, for example, for $\alpha = 0.282$ we find $\Lambda_T = 0.9660$ for $n_c = (D_c/a)(a/\Delta x) = 8 \times 0.25 = 2$ while $\Lambda_T = 1.004$ for $n_c = 4$. There is an improvement with decreasing Δx, as expected, while changing r_T/a from 1.15 to 1.08 has a very minor effect. On the other hand, too small a value of r_T/a decreases accuracy as shown comparing the last two simulations with 27 regularly arranged particles. Summarizing our experience on the influence of this parameter we can say that a good choice for r_T/a is between $1 + \Delta x/a$ and $1 + 2\Delta x/a$.

6.3. Stationary particles in a moving fluid

We now turn to the steady flow past a fixed sphere at a Reynolds number $Re = 2aU/\nu = 50$; U is the incident velocity. The momentum aspects of the PHYSALIS method have been extensively validated in our earlier papers (see e.g. [16,36]), where we also address criteria for the choice of r_s; we refer the reader to these references for details on these issues. We simply note that we have repeated some of the earlier tests, and particularly those with flow past a periodic array of spheres for which exact balance relations are available, with similar results.

Table 3
Calculated drag coefficient C_D and particle Nusselt number Nu_p for steady uniform flow past a single spherical particle at $Re = 50$ for various values of the radius r_s of the momentum integration surface, order of truncation ℓ_{max} of the infinite summations, mesh lengths per radius $a/\Delta x$ and domain size. The deviation from 1 of the quantity Λ_q, defined in (32), is a measure of the numerical error affecting the solution of the energy equation. For all these simulations, the radius of the integration surface for the temperature is $r_T/a = 1.15$ and the order of truncation in (12) $\ell_{max} = 3$.

r_s/a	ℓ_{max}	$a/\Delta x$	domain size	C_D	Nu_p	Λ_q
1.2	3	8	$20a \times 20a \times 40a$	1.6272	5.4119	1.0078
1.2	3	8	$20a \times 20a \times 40a$	1.6274	5.4123	1.0078
1.25	3	8	$20a \times 20a \times 40a$	1.6381	5.4111	1.0079
1.15	3	8	$20a \times 20a \times 40a$	1.6288	5.4130	1.0078
1.2	2	8	$20a \times 20a \times 40a$	1.6266	5.4115	1.0080
1.2	3	10	$16a \times 16a \times 32a$	1.6526	5.4548	1.0034
1.2	3	6	$20a \times 20a \times 40a$	1.6540	5.3193	1.0226

Table 4
Drag coefficient C_D and particle Nusselt number Nu_p for steady uniform flow past a single spherical particle at $Re = 50$ from the literature. The data in the first group are from numerical simulations (label "S"), those in the second one from empirical correlations (label "C"); the last line is an experimental value (label "E").

	type	$C_D(Re = 50)$	$Nu_p(Re = 50)$
Xia et al. [46]	S	1.53	5.33
Richter and Nikrityuk [30]	S	1.577	5.49
Schlichting and Gersten [32]		1.61	–
Bagchi et al. [3]	S	1.57	5.4
Mittal [23]	S	1.57	–
Tabata and Itakura [39]	S	1.579	–
Haider and Levenspiel [17]	C	1.633	–
Clift et al. [6]	C	1.57	–
Whitaker [45]	C	–	5.19
Feng and Michaelides [9]	C	–	5.51
Ranz and Marshall [28]	C	–	5.81
Roos and Willmarth [31]	E	1.60	–

Some computed results for the drag coefficient for a single sphere in steady uniform flow are shown in Table 3 for different orders of truncation and cells per radius. The computed values are seen to vary little with the parameters of the calculation. An exception are the last two entries, both of which give a somewhat larger drag coefficient than the others, one because the discretization, with $a/\Delta x = 6$, is too coarse, the other because the domain is small.

To gain some perspective on these results we show in Table 4 a collection of results from the literature. With a few exceptions, the reported values are somewhat lower than our computed values but they all agree within a few percent.

The next-to-last column of Table 3 shows the computed results for the single-particle Nusselt number Nu_p with the various parameter values used for the velocity calculation. To generate these results, in solving the energy equation we used $a/\Delta x = 8$, $r_T/a = 1.15$ and $\ell_{max} = 3$; the fluid enters the domain at the reference temperature and homogeneous Neumann conditions are imposed to the temperature field on the rest of the boundary.

By the methods demonstrated in the Appendix it is easy to show that, for flow over one or more heated bodies, at steady conditions the overall energy balance over the computational domain requires that the quantity

$$\Lambda_q = \frac{\rho c_p}{\sum_{\alpha=1}^{N_p} Q_p} \oint_{S_f} T\mathbf{u} \cdot \mathbf{n} dS_f \,, \tag{32}$$

equal 1; the summation is over all the particles in the domain. The values of Λ_q for the single-particle case are shown in the last column of Table 3. The result closest to 1 is found with the finest discretization $a/\Delta x = 10$, but all the Nusselt numbers calculated with $a/\Delta x = 8$ differ by less than 1% from this value. The error with the coarser discretization $a/\Delta x = 6$ is somewhat larger, about 2%.

Fig. 8 compares the local Nusselt number over the particle surface, defined by,

$$Nu_{loc} = -\frac{2a}{T_p} \nabla T \cdot \mathbf{n}_p \,, \tag{33}$$

with the values reported by [4]. There is a very good agreement over the entire surface of the sphere, except near the front stagnation point where one observes a difference of 4.5%. This prediction is robust with respect to variations of the parameters of our calculation; we may note that a very similar difference is reported by [46]. This result has been obtained with $r_s/a = 1.2$, $r_T/a = 1.15$, $a/\Delta x = 8$ and $\ell_{max} = 3$ for both the momentum and the energy calculation.

We also carried out a test with 10 equal particles simultaneously present in the domain, subjected to the same incident flow with $Re = 50$, having different temperatures randomly assigned between 80% and 120% of a mean temperature equal

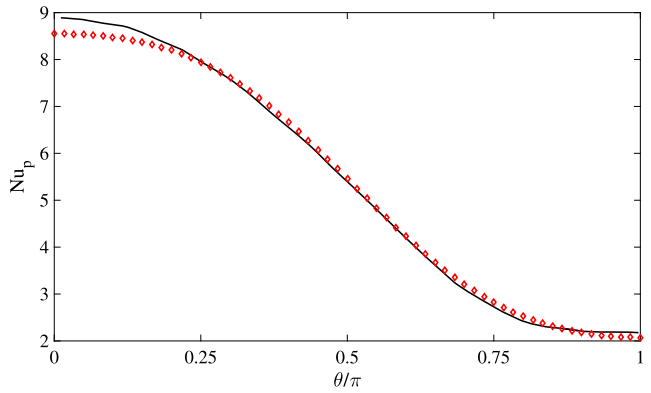

Fig. 8. The local Nusselt number, or dimensionless heat flux, defined in (33), at the surface of a sphere immersed in a steady uniform flow at a Reynolds number 50 as a function of the azimuthal angle. The solid line is the result of [4] and the points the present results.

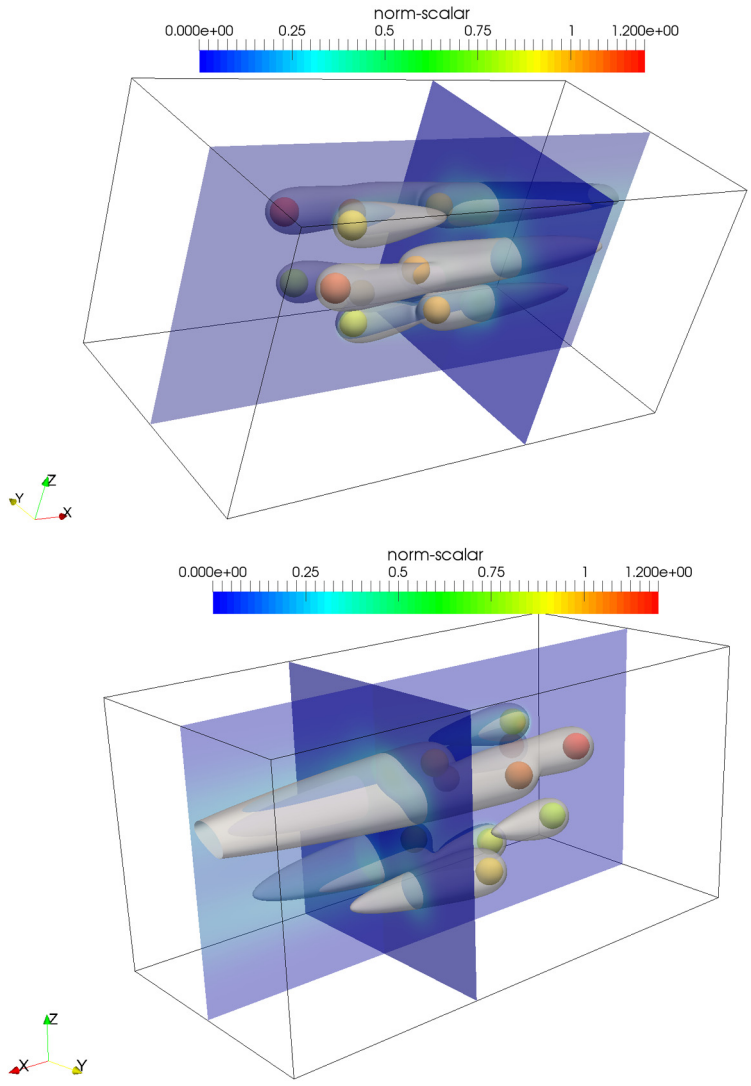

Fig. 9. Two views of the steady temperature distribution and thermal wakes produced by 10 randomly arranged particles immersed in a cold stream; the color indicates the temperature. The particle temperature is fixed and is randomly assigned between 80% and 120% of the mean value 1 and the temperature of the incoming fluid is 0.

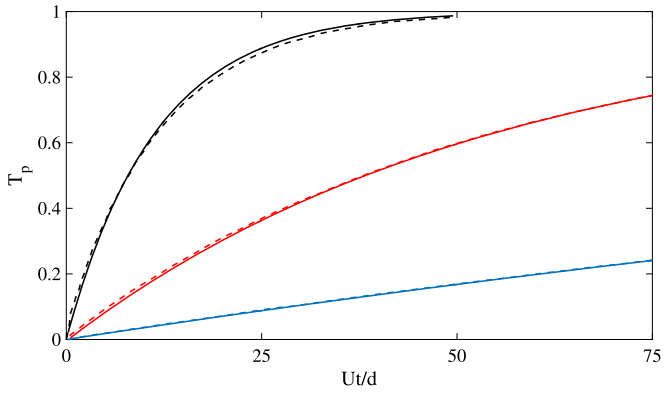

Fig. 10. Time-dependence of the temperature of a particle immersed in a warmer uniform flow with $Re = 50$. The solid lines are the present results and the dashed lines the results of [5]. The three sets of curves correspond, in ascending order, to different values of the ratio $\rho c_p/(\rho_p c_{pp}) = 0.004$, 0.02 and 0.1.

to 1; the fluid enters the domain at the reference temperature and the other boundaries are insulated. In this test we used again $a/\Delta x = 8$ and for the parameter defined in (32) found the value $\Lambda_q = 1.003$. Fig. 9 shows two views of the temperature iso-surfaces corresponding to a temperature of 0.2; the color shows the particle temperature and the temperature distribution on two orthogonal planes.

6.4. Transient heating of a sphere in a flow

For our last example we consider the transient heating of a particle exposed to a warmer incident flow with $Re = 50$. The simulation set-up was the same as in the previous steady example. All the temperature boundary conditions on the boundary of the computational domain are homogeneous-Neumann except for the inlet plane, where the temperature is held fixed at a value above the reference temperature, which is the initial temperature of the particle. We waited for steady, fully developed flow conditions to be established before allowing the particle temperature to vary according to (4); this instant is chosen as $t = 0$. The results for three values of the ratio $\rho c_p/(\rho_p c_{pp}) = 0.004$, 0.02 and 0.1 are shown in ascending order by the solid lines in Fig. 10, where they are compared with the results of [5] (dashed lines). The corresponding values of the parameter $U\tau_p/a$, with τ_p the particle time constant defined in (5), are 1458.3, 291.68 and 58.333. Here we used $\ell_{max} = 3$ for both the momentum and energy expansions, $r_s/a = 1.2$ for the momentum equation and $r_T/a = 1.15$ for the energy equation. The agreement between the two sets of results is excellent.

7. Examples with natural convection

In closing we consider a few examples with natural convection, beginning with a single-phase example. The simulation domain is a parallelepiped with a square cross section with an aspect ratio (side/height) equal to $\frac{1}{2}$. The bottom surface is heated to a temperature T_h and the top one is cooled to a temperature T_c. For the Rayleigh number, defined by

$$Ra = \frac{g\beta(T_h - T_c)L_z^3}{\nu D}, \tag{34}$$

we consider two values, $Ra = 2 \times 10^5$ and $Ra = 2 \times 10^6$; L_z is the height of the domain. In the first case the flow field is steady while, in the second one, the flow is slightly turbulent; in this latter case the results reported are time-average values obtained after stationary conditions have been reached. Table 5 shows the simulation parameters and the overall balances for the heat flux, kinetic energy dissipation and temperature dissipation; the latter two quantities are defined, respectively, by

$$\Lambda_u = \frac{\langle \Phi \rangle/\rho}{\epsilon_u} \qquad \text{and} \qquad \Lambda_\theta = \frac{D\langle |\nabla T|^2 \rangle}{\epsilon_\theta}, \tag{35}$$

with $\Phi = \rho\nu \sum_{i,j=1}^{3} (\partial u_i/\partial x_j)(\partial u_i/\partial x_j)$ the dissipation function; the angle brackets denote volume and time averages. The quantities ϵ_u and ϵ_θ are defined by the numerators of these fractions and, as proven in the Appendix, they can be related to the Nusselt numbers and other quantities of the flow as shown in (A.20) and (A.16). Thus, both Λ_u and Λ_θ should equal 1 in the absence of errors. It is noticed in Table 5 that, when the number of nodes increases, a better performance for the overall balances is obtained with errors approaching 1% or less.

In the second example, we introduce 1, 5 or 8 particles into the same domain; the Rayleigh number defined in the same way as shown in (34) is 2×10^5 and $Pr = 1.75$. For the one-particle cases the particle temperature is fixed above or below the reference temperature taken as $T_{ref} = \frac{1}{2}(T_h + T_c) = 0$. In the other two cases the particles are randomly distributed

Table 5
Overall energy balance for single-phase natural convection for two values of the Rayleigh number Ra and Prandtl number Pr and different domain discretizations. The convection cell is a parallelepiped with a square cross section and aspect ratio (side/height) = 1/2; N_x, N_y and N_z are the number of grid points in the two horizontal and the vertical directions; the Nusselt number shown is $Nu = \frac{1}{2}(Nu_c + Nu_h)$. The quantities in the last three columns should all be equal to 1 in the absence of errors; Λ_u is the ratio of the computed kinetic energy dissipation rate to the theoretical result given in (A.20); Λ_θ is the ratio of the temperature dissipation rate to the theoretical result given in (A.16). Note that in the work of [37], the convection cell is a cylinder rather than a parallelepiped and the numbers of cells quoted are in the azimuthal, radial and axial directions.

	Ra	Pr	$N_x \times N_y \times N_z$	Nu	Nu_h/Nu_c	Λ_u	Λ_θ
Present	2×10^5	1.75	$50 \times 50 \times 100$	5.163	1.000	0.955	0.996
Present	2×10^5	1.75	$65 \times 65 \times 130$	5.162	1.000	0.972	0.998
Present	2×10^6	0.7	$65 \times 65 \times 130$	11.510	0.998	0.903	0.979
Present	2×10^6	0.7	$75 \times 75 \times 150$	11.485	0.999	0.924	0.985
Present	2×10^6	0.7	$100 \times 100 \times 200$	11.216	0.998	0.955	0.993
Present	2×10^6	0.7	$110 \times 110 \times 220$	11.556	1.005	0.961	0.994
Stevens et al.	2×10^6	0.7	$97 \times 49 \times 129$	10.32	–	0.973	0.978
Stevens et al.	2×10^6	0.7	$193 \times 97 \times 257$	11.03	–	0.974	0.991

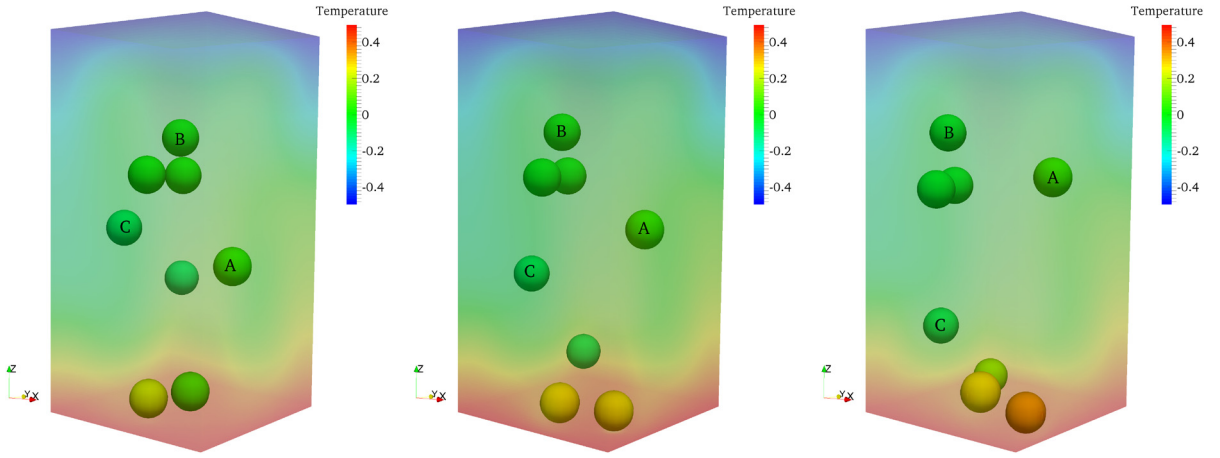

Fig. 11. Successive configurations of an eight-particle system in naturally convecting flow with $Ra = 2 \times 10^5$ and $Pr = 1.75$; the color indicates the temperature normalized by $T_h - T_c$, which ranges from -0.5 at the bottom to 0.5 at the top of the cell. The frames are separated by a dimensionless time interval $\sqrt{g\beta(T_h - T_c)L_z}\,\Delta t/L_z \simeq 2.07$. The particle temperature adjusts according to (4); $\rho c_p/(\rho_p c_{pp}) = 0.1$. Note the response of the particles to the recirculating motion established by the natural convection in the cell as well as their changing temperature.

and the particle temperature is also fixed and randomly assigned in the range shown in Table 6; Λ_u and Λ_θ are as defined before, while the quantity Λ_{Nu} is defined as

$$\Lambda_{Nu} \equiv \frac{kS_f(T_h - T_c)}{L_z} \frac{Nu_c - Nu_h}{\sum_{\alpha=1}^{N_p} Q^\alpha}, \tag{36}$$

and should equal 1 in the absence of errors (see Appendix). Here Nu_c and Nu_h are the Nusselt numbers at the cold and hot bases of the computational cell defined by

$$Nu_{h,c} = -\frac{L_z}{T_h - T_c} \left\langle \frac{\partial T}{\partial z} \right\rangle \Big|_{z=0,L_z}, \tag{37}$$

in which angle brackets denote averages over the bases of the cell (and also over time for $Ra = 2 \times 10^6$). These results were obtained by using $r_s/a = 1.2$, $r_T/a = 1.15$ and $\ell_{max} = 3$ for both the momentum and temperature expansions. In all cases Λ_{Nu} and Λ_θ deviate from the exact value 1 by much less than 1%. The deviation of Λ_u from 1 is somewhat greater but always less than 5% and is seen to decrease as the number of nodes is increased.

In the last example, we allow 8 particles to translate and rotate freely for a case with parameters chosen so that $Ra = 2 \times 10^5$ and $Pr = 1.75$ as for the fixed-particles cases. The particles adjust their temperature according to (4). The values of the other parameters are $\rho_p/\rho = 70$ and $\rho c_p/(\rho_p c_{pp}) = 0.1$; the calculation was carried out with $a/\Delta x = 8$, $r_s/a = 1.2$, $r_T/a = 1.15$ and $\ell_{max} = 3$ for both the momentum and energy expansions. Fig. 11, where color indicates the temperature, shows three snapshots of the system. One notices the motion of the particles as they are carried around the cell by the circulating natural convection flow and their varying temperature. The video sequence from which these three stills are taken is available as Supplementary Material in the on-line version of this paper.

Table 6
Natural convection with N_p fixed particles and $Ra = 2 \times 10^5$, $Pr = 1.75$. The convection cell is a parallelepiped with a square cross section and aspect ratio (side/height) = 1/2; N_x, N_y and N_z are the number of grid points in the two horizontal and the vertical directions. The quantities in the last three columns should all be equal to 1 in the absence of errors; Λ_{Nu} is the normalized heat-flux balance given in (36); Λ_u is the ratio of the computed kinetic energy dissipation rate to the theoretical result given in (A.20); Λ_θ is the ratio of the temperature dissipation rate to the theoretical result given in (A.16). In the multi-particle cases, the particle position is randomly assigned and the particle temperature randomly fixed in the range shown.

Nu_c	Nu_h	N_p	L_z/a	$T_p/(T_h - T_c)$	$N_x \times N_y \times N_z$	Λ_{Nu}	Λ_u	Λ_θ
5.745	4.534	1	13.3	0.2	$50 \times 50 \times 100$	1.0016	0.9564	0.9937
4.881	5.506	1	13.3	-0.1	$50 \times 50 \times 100$	0.9934	0.9558	0.9951
3.309	5.844	5	20.0	$-0.5 \sim 0$	$80 \times 80 \times 160$	0.9985	0.9749	0.9906
4.797	4.567	8	20.0	$-0.35 \sim 0.35$	$80 \times 80 \times 160$	0.9962	0.9826	0.9847

It follows from (A.15) in the Appendix that the quantity defined by the generalization of (36) to the unsteady case:

$$\Lambda_\theta = \frac{D\langle|\nabla T|^2\rangle}{\epsilon_\theta + \frac{d}{dt}\int_{V_f} \frac{1}{2}\theta^2 dV_f}, \tag{38}$$

with $\theta = T - \frac{1}{2}(T_h + T_c)$, should equal 1. We find that this balance differs from 1 by about 5% for the duration of the simulation, although we observe fairly strong deviations when particles get close to the hot or cold cell bases. This is due to the fairly coarse procedure that we have adopted for simplicity to estimate the temperature gradient at the cell bases for use in the definitions (37) (of course, the temperature gradients at the particle surfaces are calculated from the expansion (15) as stated previously).

8. Summary and conclusions

We have extended to the energy equation the basic idea underlying the PHYSALIS algorithm, namely the use of local solutions as bridges between the particle surface and the fixed grid. This has permitted us to carry out fully-resolved simulations of moving particles exchanging energy, as well as momentum, with the surrounding fluid. We have demonstrated the method for several situations for which the use of integral balances gives exact results. In this way we were led to the conclusion that the numerical errors of our procedure do not exceed a few percent at most and decrease as the grid is refined. For many quantities, the errors were much less than 1%. Just as in the isothermal case considered in earlier papers, the method gives accurate results even with fairly coarse discretizations. Important quantities, such as the particle Nusselt number, do not require separate calculations but are found directly in the course of the solution procedure, almost as a by-product of the algorithm.

We considered a fluid with constant properties, but treated also examples with natural convection in the Boussinesq approximation. For the particles we assumed a lumped-capacitance model, and we have pointed out how more general thermal properties can be handled in a similar way.

The spatial discretization is second-order accurate in space but, due to the use of linear interpolation in the calculation of the scalar products (7) and (16), the overall accuracy is somewhat reduced. The explicit time stepping procedure results in a first-order accuracy in time, although more accurate implementations can readily be devised.

Mathematically, the energy equation is parabolic just as other important equations, such as the one governing mass diffusion. Thus, the same method can be used for dissolving or accreting particles, as long as they can be assumed to remain spherical. Another situation that can be addressed in the same way is, for example, the absorption of an organic pollutant dissolved in water by activated carbon particles. Our experience with the momentum equation suggests that it may be equally possible to treat problems governed by non-linear parabolic equations.

Acknowledgements

This work has been supported by NSF under grant CBET 1335965.

Appendix A. Integral balances

We give here a derivation of the integral balances used in the validation of the method in sections 6 and 7. These relations are well-known in the theory of single-phase Rayleigh–Bénard convection (see e.g. [1]), but the presence of particles modifies them so that it is worth while to present a specific derivation for this case.

We consider a computational domain in the form of a parallelepiped with or without N_p spherical particles, fixed or mobile, in its interior. The velocity boundary conditions on the surface S_f of the parallelepiped enforce inflow/outflow, no-slip or periodicity. In the absence of natural convection effects, we assume a prescribed temperature, periodicity or insulation conditions on S_f. When natural convection effects are accounted for, no-slip applies over the entire S_f and insulation conditions apply on the lateral portion of S_f while the lower and upper bases, S_h and S_c, are at constant uniform temperatures T_h and T_c, respectively; the z-axis is taken parallel to the acceleration of gravity and directed upward. The derivations apply specifically to these conditions.

In the derivation we make use of the extended Reynolds's transport theorem for a generic quantity ϕ applicable to a fluid domain the boundary of which is in arbitrary motion:

$$\frac{d}{dt}\int_{V_f}\phi dV_f = \int_{V_f}\frac{\partial\phi}{\partial t}dV_f + \oint_{S_t}\phi\mathbf{v}\cdot\mathbf{n}dS_t\,. \tag{A.1}$$

Here V_f is the volume occupied by the fluid and S_t the total boundary of this volume consisting, in the present application, of the particle surfaces and of the external boundary S_f of the computational domain. The quantity ϕ satisfies a general balance equation of the form

$$\frac{\partial\phi}{\partial t} + \mathbf{u}\cdot\nabla\phi = \nabla\cdot\mathbf{j} + \Sigma\,, \tag{A.2}$$

with $\mathbf{j}$ the flux of ϕ and Σ its volume source. Upon using this equation and the divergence theorem, (A.1) may be written as

$$\frac{d}{dt}\int_{V_f}\phi dV_f = \oint_{S_t}\phi(\mathbf{v}-\mathbf{u})\cdot\mathbf{n}dS_t + \oint_{S_f}\mathbf{j}\cdot\mathbf{n}dS_t + \int_{V_f}\Sigma dV_f\,. \tag{A.3}$$

We now specialize this relation to the problem at hand recognizing that, on the particle surfaces, $(\mathbf{v}-\mathbf{u})\cdot\mathbf{n} = 0$ while, on the outer surface, $\mathbf{v} = 0$. Thus the equation becomes

$$\frac{d}{dt}\int_{V_f}\phi dV_f = \oint_{S_f}(\mathbf{j}-\phi\mathbf{u})\cdot\mathbf{n}dS_f - \sum_{\alpha=1}^{N_p}\oint_{s_p^\alpha}\mathbf{j}\cdot\mathbf{n}_p^\alpha ds_p^\alpha + \int_{V_f}\Sigma dV_f\,. \tag{A.4}$$

Here $\mathbf{n}_p^\alpha$ is the unit normal outwardly directed on the surface s_p^α of the α-th particle.

If we apply this relation to the energy equation (3) we have

$$\frac{d}{dt}\int_{V_f}TdV_f = -\oint_{S_f}(D\nabla T + T\mathbf{u})\cdot\mathbf{n}dS_f + \sum_{\alpha=1}^{N_p}\oint_{s_p^\alpha}D\nabla T\cdot\mathbf{n}_p^\alpha ds_p^\alpha\,. \tag{A.5}$$

With the boundary conditions specified above, the contribution of the convection term to the integral over S_f vanishes. The contribution of ∇T to the integral over the lateral surfaces of S_f also vanishes so that the first integral in the right-hand side reduces to

$$\oint_{S_f}\nabla T\cdot\mathbf{n}dS_f = \int_{S_h}\nabla T\cdot\mathbf{n}_h dS_h + \int_{S_c}\nabla T\cdot\mathbf{n}_c dS_c\,. \tag{A.6}$$

We define the Nusselt number on the lower surface as the normalized heat flux into the computational domain:

$$Nu_h = \frac{L_z}{S_h(T_h-T_c)}\int_{S_h}\nabla T\cdot\mathbf{n}_h dS_h\,, \tag{A.7}$$

with L_z the vertical extent of the domain, and on the upper surface as the normalized heat flux out of the computational domain:

$$Nu_c = -\frac{L_z}{S_c(T_h-T_c)}\int_{S_c}\nabla T\cdot\mathbf{n}_c dS_c\,. \tag{A.8}$$

If $T_h = T_c$, both Nusselt numbers are defined to vanish. With these definitions, since the surface areas of the lower and upper horizontal surfaces are equal, (A.6) becomes

$$\oint_{S_f}\nabla T\cdot\mathbf{n}dS_f = -\frac{S_h}{L_z}(T_h-T_c)(Nu_c-Nu_h) \tag{A.9}$$

and (A.5) itself reduces to

$$\frac{d}{dt}\int_{V_f}TdV_f = -\frac{DS_h}{L_z}(T_h-T_c)(Nu_c-Nu_h) - \frac{1}{k}\sum_{\alpha=1}^{N_p}Q^\alpha\,, \tag{A.10}$$

where

$$Q^{\alpha} = -\oint_{s_p^{\alpha}} k\nabla T \cdot \mathbf{n}_p^{\alpha} ds_p^{\alpha}, \tag{A.11}$$

is the heat flow out of the α-th particle. In particular, without particles and in steady conditions (A.10) reduces to $Nu_h = Nu_c$ as expected. In steady conditions and in the presence of particles we deduce form this relation that the quantity Λ_{Nu} defined in (36) should equal 1.

Another test that can be based on the steady-state version of (A.5) concerns a single stationary particle at a fixed temperature in an enclosure with walls at a uniform, different fixed temperature in the absence of flow. In this case conservation of energy requires that the ratio

$$\Lambda_T = \frac{\oint_{S_p} \nabla T \cdot \mathbf{n}_p ds_p}{\int_{S_f} \nabla T \cdot \mathbf{n} dS_f}, \tag{A.12}$$

be equal to 1. We have used this result in the first two examples of section 6.

The so-called thermal, or temperature, dissipation is defined as the integral over the fluid volume of $k|\nabla\theta|^2$ with $\theta = T - \frac{1}{2}(T_h + T_c)$. A balance equation for the square of this quantity readily follows from the energy equation and is

$$\frac{\partial}{\partial t}\frac{1}{2}\theta^2 + \mathbf{u}\cdot\nabla\frac{1}{2}\theta^2 = D\left[\nabla(\theta\nabla\theta) - |\nabla\theta|^2\right]. \tag{A.13}$$

In this case, therefore, the general equation (A.4) becomes

$$\frac{d}{dt}\int_{V_f}\frac{1}{2}\theta^2 dV_f + D\oint_{S_f}\theta\nabla\theta\cdot\mathbf{n}dS_f - D\sum_{\alpha=1}^{N_p}\oint_{s_p^{\alpha}}\theta\nabla\theta\cdot\mathbf{n}_p^{\alpha}ds_p^{\alpha} = D\int_{V_f}|\nabla\theta|^2 dV_f. \tag{A.14}$$

In writing this equation the convective term has been omitted since it vanishes with the boundary conditions that we consider. Thus we find

$$D\int_{V_f}|\nabla\theta|^2 dV_f = \frac{d}{dt}\int_{V_f}\frac{1}{2}\theta^2 dV_f + \frac{DS_h(T_h-T_c)^2}{2L_z}(Nu_h + Nu_c) + \frac{D}{k}\sum_{\alpha=1}^{N_p}\theta_p^{\alpha}Q^{\alpha} \tag{A.15}$$

in writing which we have used the fact that $\theta = \theta_p^{\alpha}$ is a constant over the surface of the α-th particle; here Nu_h and Nu_c denote instantaneous values. After reaching statistically steady conditions we have

$$\epsilon_\theta = \frac{D(T_h-T_c)^2}{2L_z^2}(Nu_c + Nu_h) + \frac{D}{V_f k}\sum_{\alpha=1}^{N_p}\theta_p^{\alpha}Q^{\alpha}, \tag{A.16}$$

in which $\epsilon_\theta = k\langle|\nabla\theta|^2\rangle$ is the volume and time average of $k|\nabla\theta|^2$.

The final balance relation concerns the integral of the total energy $\mathcal{E} = \frac{1}{2}\rho u^2 + \rho\beta\mathbf{x}\cdot\mathbf{g}T$ given by the sum of the kinetic and potential energies. Upon using the momentum and energy equations (2) and (3) we find

$$\frac{\partial\mathcal{E}}{\partial t} + \mathbf{u}\cdot\nabla\mathcal{E} = \nabla\cdot[\mathbf{u}\cdot\boldsymbol{\sigma} + \rho\beta(\mathbf{x}\cdot\mathbf{g})\nabla T - T\mathbf{g}] - \Phi \tag{A.17}$$

in which $\boldsymbol{\sigma}$ is the total stress and $\Phi = \rho\nu(\partial u_j/\partial x_i)(\partial u_j/\partial x_i)$ is the dissipation function. The flux $\mathbf{j}$ and volume source Σ appearing in (A.4) can be read off from this relation and substituted into (A.4). The convective terms vanish by the boundary conditions and we are left with

$$\begin{aligned}\frac{d}{dt}\int_{V_f}\mathcal{E}dV_f = {}& \rho\beta D\oint_{S_f}[(\mathbf{x}\cdot\mathbf{g})\nabla T - T\mathbf{g}]\cdot\mathbf{n}dS_f \\ & - \sum_{\alpha=1}^{N_p}\oint_{s_p^{\alpha}}[\mathbf{u}\cdot\boldsymbol{\sigma} + \rho\beta D(\mathbf{x}\cdot\mathbf{g})\nabla T]\cdot\mathbf{n}_p^{\alpha}ds_p^{\alpha} - \int_{V_f}\Phi dV_f,\end{aligned} \tag{A.18}$$

where terms that do not contribute have been omitted. The result takes on a slightly simpler form if the origin is taken at the center of the domain so that the z coordinates of the two bases are $\pm\frac{1}{2}L_z$. With this choice we find

$$\int_{V_f} \Phi dV_f = -\frac{d}{dt}\int_{V_f} \mathcal{E} dV_f + \rho\beta D g S_h (T_h - T_c)\left[\frac{1}{2}(Nu_h + Nu_c) - 1\right] - \sum_{\alpha=1}^{N_p}\left[\mathbf{w}^\alpha \cdot \mathbf{F}^\alpha + \mathbf{\Omega}^\alpha \cdot \mathbf{L}^\alpha + \rho\beta D \oint_{s_p^\alpha} (\mathbf{x}\cdot\mathbf{g})\nabla T \cdot \mathbf{n}_p^\alpha ds_p^\alpha\right], \tag{A.19}$$

in which $g = |\mathbf{g}|$ and $\mathbf{F}^\alpha$ and $\mathbf{L}^\alpha$ are the hydrodynamic forces and couples on the particles. In statistically steady conditions this result may be written as

$$\epsilon_u = \frac{\nu^3 Ra}{L_z^4 Pr^2}\left[\frac{1}{2}(Nu_h + Nu_c) - 1\right] - \frac{1}{V_f \rho}\sum_{\alpha=1}^{N_p}\left[\mathbf{w}^\alpha \cdot \mathbf{F}^\alpha + \mathbf{\Omega}^\alpha \cdot \mathbf{L}^\alpha + \rho\beta D \oint_{s_p^\alpha} (\mathbf{x}\cdot\mathbf{g})\nabla T \cdot \mathbf{n}_p^\alpha ds_p^\alpha\right], \tag{A.20}$$

in which $\epsilon_u = \langle \Phi/\rho \rangle$ is the volume and time average of Φ/ρ.

Appendix B. Supplementary material

Supplementary material related to this article can be found online at http://dx.doi.org/10.1016/j.jcp.2017.07.044.

References

[1] G. Ahlers, S. Grossmann, D. Lohse, Heat transfer and large scale dynamics in turbulent Rayleigh–Bénard convection, Rev. Mod. Phys. 81 (2009) 503–537.
[2] B. Arcen, A. Taniére, M. Khalij, Heat transfer in a turbulent particle-laden channel flow, Int. J. Heat Mass Transf. 55 (2012) 6519–6529.
[3] P. Bagchi, M.Y. Ha, S. Balachandar, Direct numerical simulation of flow and heat transfer from a sphere in a uniform cross-flow, J. Fluids Eng. 123 (2001) 347–358.
[4] P. Bagchi, M.Y. Ha, S. Balachandar, Direct numerical simulation of flow and heat transfer from a sphere in a uniform cross-flow, J. Fluids Eng. Trans. ASME 123 (2001) 347–358.
[5] S. Balachandar, M.Y. Ha, Unsteady heat transfer from a sphere in a uniform cross-flow, Phys. Fluids 13 (2001) 3714.
[6] R. Clift, J. Grace, M. Weber, Bubbles, Drops, and Particles, Academic Press, 1978.
[7] N.G. Deen, S.H.L. Kriebitzsch, M.A. van der Hoef, J.A.M. Kuipers, Direct numerical simulation of flow and heat transfer in dense fluid–particle systems, Chem. Eng. Sci. 81 (2012) 329–344.
[8] N.G. Deen, M. van Sint Annaland, M.A. van der Hoef, J.A.M. Kuipers, Review of discrete particle modeling of fluidized beds, Chem. Eng. Sci. 62 (2007) 28–44.
[9] Z.G. Feng, E.E. Michaelides, A numerical study on the transient heat transfer from a sphere at high Reynolds and Péclet numbers, Int. J. Heat Mass Transf. 43 (2000) 219–229.
[10] Z.-G. Feng, E.E. Michaelides, Inclusion of heat transfer computations for particle laden flows, Phys. Fluids 20 (2008) 040604.
[11] Z.-G. Feng, E.E. Michaelides, Heat transfer in particulate flows with direct numerical simulation (DNS), Int. J. Heat Mass Transf. 52 (2009) 777–786.
[12] Z.G. Feng, S.G. Musong, Direct numerical simulation of heat and mass transfer of spheres in a fluidized bed, Powder Technol. 262 (2014) 62–70.
[13] W. Fornari, A. Formenti, F. Picano, L. Brandt, The effect of particle density in turbulent channel flow laden with finite size particles in semi-dilute conditions, Phys. Fluids 28 (2016) 033301.
[14] M. Garcia-Villalba, A.G. Kidanemariam, M. Uhlmann, DNS of vertical plane channel flow with finite-size particles: Voronoi analysis, acceleration statistics and particle-conditioned averaging, Int. J. Multiphase Flow 46 (2012) 54–74.
[15] R. Glowinski, T.-W. Pan, T.I. Hesla, D.D. Joseph, J. Periaux, A fictitious domain approach to the direct numerical simulation of incompressible viscous flow past moving rigid bodies: application to particulate flow, J. Comput. Phys. 169 (2001) 363–426.
[16] K. Gudmundsson, A. Prosperetti, Improved procedure for the computation of Lamb's coefficients in the Physalis method for particle simulation, J. Comput. Phys. 234 (2013) 44–59.
[17] A. Haider, O. Levenspiel, Drag coefficient and terminal velocity of spherical and nonspherical particles, Powder Technol. 58 (1989) 63–70.
[18] T. Kempe, J. Froehlich, An improved immersed boundary method with direct forcing for the simulation of particle laden flows, J. Comput. Phys. 231 (2012) 3663–3684.
[19] A.G. Kidanemariam, M. Uhlmann, Direct numerical simulation of pattern formation in subaqueous sediment, J. Fluid Mech. 750 (2014) R2.
[20] S. Kim, S.J. Karrila, Microhydrodynamics: Principles and Selected Applications, Butterworth–Heinemann, Boston, MA, 1991.
[21] H. Kruggel-Emden, B. Kravets, M.K. Suryanarayana, R. Jasevicius, Direct numerical simulation of coupled fluid flow and heat transfer for single particles and particle packings by a LBM-approach, Powder Technol. 294 (2016) 236–251.
[22] H. Lamb, Hydrodynamics, 6th edition, Dover, New York, NY, 1932.
[23] R. Mittal, A Fourier–Chebyshev spectral collocation method for simulating flow past spheres and spheroids, Int. J. Numer. Methods Fluids 30 (1999) 921–937.
[24] R. Mittal, H. Dong, M. Bozkurttas, F.M. Najjar, A. Vargas, A. von Loebbecke, A versatile sharp interface immersed boundary method for incompressible flows with complex boundaries, J. Comput. Phys. 227 (2008) 4825–4852.
[25] A. Noorani, G. Sardina, L. Brandt, P. Schlatter, Particle transport in turbulent curved pipe flow, J. Fluid Mech. 793 (2016) 248–279.
[26] F. Picano, W.-P. Breugem, L. Brandt, Turbulent channel flow of dense suspensions of neutrally buoyant spheres, J. Fluid Mech. 764 (2015) 463–487.
[27] A. Prosperetti, H.N. Oğuz, Physalis: a new $o(n)$ method for the numerical simulation of disperse systems. Part I: Potential flow of spheres, J. Comput. Phys. 167 (2001) 196–216.
[28] W.E. Ranz, W.R. Marshall, Evaporation from drops, Part II, Chem. Eng. Prog. 48 (1952) 173–180.
[29] S. Ray, T. Kempe, J. Froehlich, Efficient modelling of particle collisions using a non-linear viscoelastic contact force, Int. J. Multiph. Flow 76 (2015) 101–110.
[30] A. Richter, P. Nikrityuk, Drag forces and heat transfer coefficients for spherical, cuboidal and ellipsoidal particles in cross flow at sub-critical Reynolds numbers, Int. J. Heat Mass Transf. 55 (2012) 1343–1354.
[31] F. Roos, W. Willmarth, Some experimental results on sphere and disk drag, AIAA J. 9 (1971) 285–291.

[32] H. Schlichting, K. Gersten, Boundary-Layer Theory, Springer Science & Business Media, 2003.
[33] J.H. Seo, R. Mittal, A high-order immersed boundary method for acoustic wave scattering and low-Mach number flow-induced sound in complex geometries, J. Comput. Phys. 230 (2011) 1000–1019.
[34] S.K. Shin, Y.A. Hassan, A direct-forcing immersed boundary method for the thermal lattice Boltzmann method, Comput. Fluids 49 (2011) 36–45.
[35] A.J. Sierakowski, GPU-centric resolved-particle disperse two-phase flow simulation using the Physalis method, Phys. Commun. 207 (2016) 24–35.
[36] A.J. Sierakowski, A. Prosperetti, Resolved-particle simulation by the Physalis method: enhancements and new capabilities, J. Comput. Phys. 309 (2016) 164–184.
[37] R.J.A.M. Stevens, R. Verzicco, D. Lohse, Radial boundary layer structure and Nusselt number in Rayleigh–Bénard convection, J. Fluid Mech. 643 (2010) 495–507.
[38] B. Sun, S. Tenneti, S. Subramaniam, D.L. Koch, Pseudo-turbulent heat flux and average gas-phase conduction during gas–solid heat transfer: flow past random fixed particle assemblies, J. Fluid Mech. 798 (2016) 299–349.
[39] M. Tabata, K. Itakura, A precise computation of drag coefficients of a sphere, Int. J. Comput. Fluid Dyn. 9 (1998) 303–311.
[40] H. Tavassoli, S.H.L. Kriebitzsch, M.A. van der Hoef, E.A.J.F. Peters, J.A.M. Kuipers, Direct numerical simulation of particulate flow with heat transfer, Int. J. Multiph. Flow 57 (2013) 29–37.
[41] S. Tenneti, B. Sun, R.S.S. Garg, Role of fluid heating in dense gas–solid flow as revealed by particle-resolved direct numerical simulation, Int. J. Heat Mass Transf. 58 (2013) 471–479.
[42] M. Uhlmann, An immersed boundary method with direct forcing for the simulation of particulate flows, J. Comput. Phys. 209 (2005) 448–476.
[43] A. Wachs, A. Hammouti, G. Vinay, M. Rahmani, Accuracy of finite volume/staggered grid distributed Lagrange multiplier/fictitious domain simulations of particulate flows, Comput. Fluids 115 (2015) 154–172.
[44] Z. Wang, J. Fan, K. Luo, K. Cen, Immersed boundary method for the simulation of flows with heat transfer, Int. J. Heat Mass Transf. 52 (2009) 4510–4518.
[45] S. Whitaker, Forced convection heat transfer correlations for flow in pipes, past flat plates, single cylinders, single spheres, and for flow in packed beds and tube bundles, AIChE J. 18 (1972) 361–371.
[46] J. Xia, K. Luo, J. Fan, A ghost-cell based high-order immersed boundary method for inter-phase heat transfer simulation, Int. J. Heat Mass Transf. 75 (2014) 302–312.
[47] J. Xia, K. Luo, J. Fan, Simulating heat transfer from moving rigid bodies using high-order ghost-cell based immersed-boundary method, Int. J. Heat Mass Transf. 89 (2015) 856–865.
[48] X.L. Yin, D.L. Koch, Velocity fluctuations and hydrodynamic diffusion in finite-Reynolds-number sedimenting suspensions, Phys. Fluids 20 (2008) 043305.
[49] F. Zonta, C. Marchioli, A. Soldati, Time behavior of heat fluxes in thermally coupled turbulent dispersed particle flows, Acta Mech. 218 (2011) 367–373.